About the Reliability of Numerical Simulated Time Dependent Current and Torque Courses of Converter Fed Induction Motors

C. Grabner

***Abstract* — Undesired secondary effects occurring at inerter-fed squirrel cage induction motors are investigated by a transient two-dimensional finite element analysis with coupled electrical circuits. Calculated time-dependent numerical courses are compared to measured ones. A novel and deeper insight into the invoked harmonic spectrum of the electrical stator current and the mechanical torque at the rotating shaft is given.**

***Keywords* — Finite element method; coupled circuits; inverter topology; induction motor.**

I. Introduction

Electrical drive systems applied for very simple industrial pump, fan or compressor applications require different torque/speed profiles in different operational states [1]. This is often realized by robust and reliable converter-fed squirrel cage induction motors as depicted in Fig.1.

The used V/f control technology needs thereby a voltage magnitude variation in dependency on the drive frequency as it is exemplarily shown in Fig.2. The section with continuously rising effective voltage up to the maximum level of 200 V at 50 Hz permits in the quasi-steady operational state almost a constant mechanical torque of 4.9 Nm, whereas the interval with constant maximal effective voltage magnitude is denoted as field weakening range, characterized with a constant mechanical power output of 770 W.

Figure 1. Family of variable speed drive systems consisting of induction motors with according power converters.

Manuscript received December 4, 2007.

Christian Grabner is with the Research and Development Department of Drive Systems, Siemens AG, Frauenauracherstrasse 80, D-91056 Erlangen, Germany, (phone: +49 162 2515841, e-mail: grabner.christian@siemens.com).

The desired high quality of the drive system is very sensitive to appearing higher harmonics in the electrical stator current or in the mechanical torque, even from unsuitable machine designs or inappropriate power converter strategies [2,3].

Such undesired current harmonics in converter driven motors can cause unforeseen losses and lead directly to additional heating effects inside the semiconductors and the winding system [4]. Mechanical problems regarding the rotating shaft can in particularly arise whenever frequencies in the generated mechanical torque spectrum coincide with natural resonance frequencies of the rotating shaft [5].

The application of different commercial calculation tools within the design process of electrical drive systems gains crucial interest in order to overcome such problems. An extended finite element method with directly coupled electrical circuits for instance allows the treatment of the complete drive system in the time-domain. Thereby, the converter topology is included by discrete electronic devices, whereas the induction motor is basically represented by iron laminations, insulation, stator winding and squirrel cage. The procedure overcomes previous insufficiencies and delivers results in dependency on well known control strategies with good accuracy.

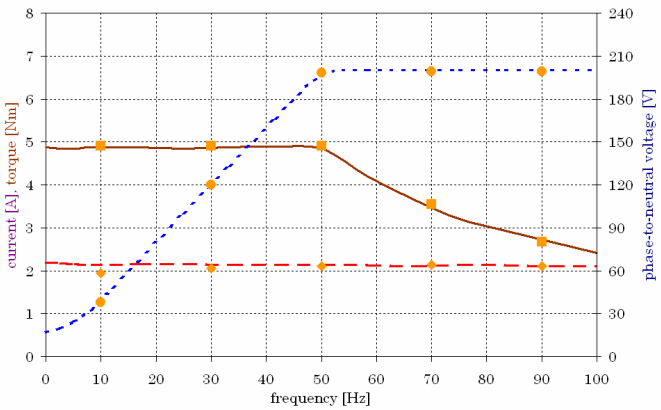

Figure 2. Measured (solid, dashed, dotted line) and numerical calculated (quadrates, circles) effective voltage (blue), effective current (magenta) and mechanical torque (brown) versus the supply frequency for the steady-state S1-duty.

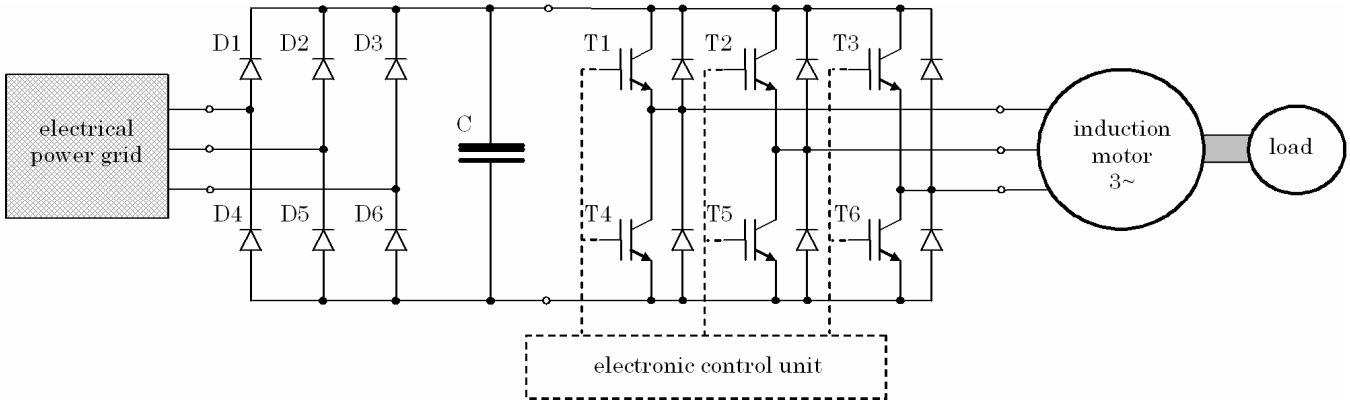

Figure 3. The simplified converter model consists of the input B6 rectifier with diodes D1 to D6, the dc voltage link, three half-bridges formed by semiconductors T1-T4, T2-T5 and T3-T6 and an electronic control unit.

II. Converter Topology and Control Unit

The power conversion from the public three-phase ac grid of constant frequency and voltage amplitude into an arbitrary three-phase ac system with variable settings is performed by means of the power converter topology in Fig.3. The input ac to dc rectification is done by the diodes D1 to D6. The classical B6-bridge causes thereby an unavoidable voltage ripple. The capacitor C smoothes these distinct fluctuations within the dc link level of $U_{ZK} \approx 565$ V, whereas the inductance L restricts undesired current peaks during unexpected operational states [6]. The conversion of the dc link to three-phase output ac power is exclusively performed in the switched mode.

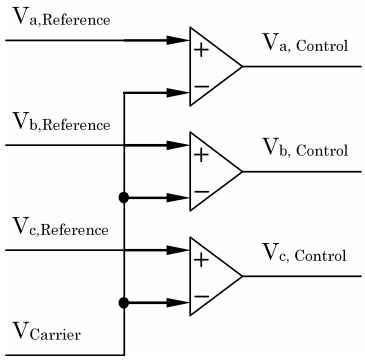

Figure 4. Sampling of reference signals by a carrier signal.

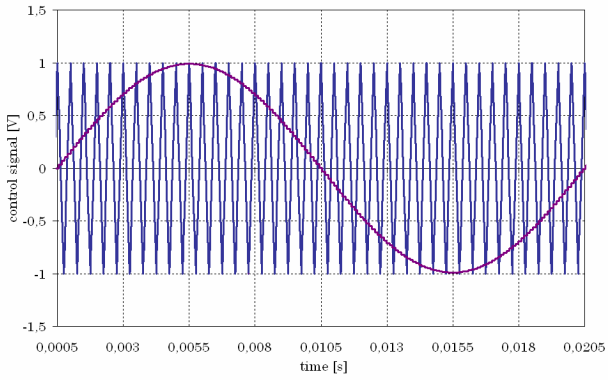

Figure 5. Saw-tooth carrier signal (blue) with 2 kHz and the sinusoidal reference signal (magenta) with 50 Hz.

The control unit in Fig.3 has the task to generate different duty cycles for the semiconductor devices T1 to T6. The most widely used method of pulse-width modulation employs carrier modulators in each of the three phases [7-9]. A simple realization of the main control part is shown in Fig.4. The according time-dependent signal courses in the control unit are exemplarity depicted in Fig.5 for the maximum output voltage at the frequency of 50 Hz. The phase reference signal with the desired drive frequency 50 Hz is thereby sampled by a single saw-tooth carrier signals with a rate of 2 kHz. The electronic control unit generates signals for the semiconductors whenever the sine-wave and saw-tooth signal have the same value.

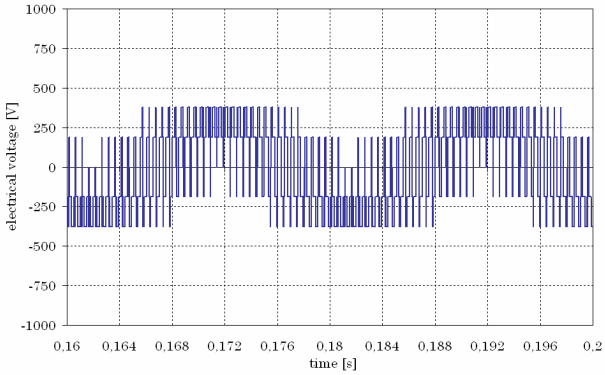

Figure 6. Switched phase-to-neutral voltage of the star-connected motor for a carrier frequency of 2 kHz.

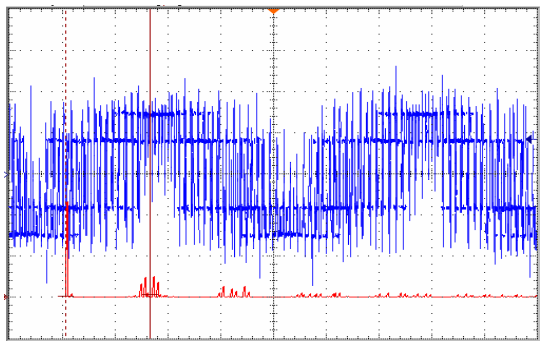

Figure 7. Measured phase-to-neutral voltage (blue) of the star-connected motor for a carrier frequency of 2 kHz, whereby one division corresponds to 4 ms in the abscissa and 250 V in the ordinate. The Fourier spectrum (red) is based on 140 V per ordinate division.

The utilized semiconductors effectuate temporary connections at high repetition rates with short rising times. The generated time-dependent phase-to-neutral output voltage in case of the used control method from Fig.4 shows within the numerical processed course in Fig.6 five distinct voltage levels. The fundamental content of the effective motor voltage is thereby 200 V at 50 Hz, as it was required for that specific steady operational state in Fig.2. The numerical calculation uses idealized switches within the power converter and neglects the motor feed cable in Fig.3.

The measured courses in Fig.7 look slightly different to that in Fig.6 because of the non-ideal effects of the motor feed cable and additionally appearing capacitive influences of the complete stator winding system. Some distinct voltage peaks are obvious in Fig.7 due to voltage reflection at the motor terminals without using additional filters.

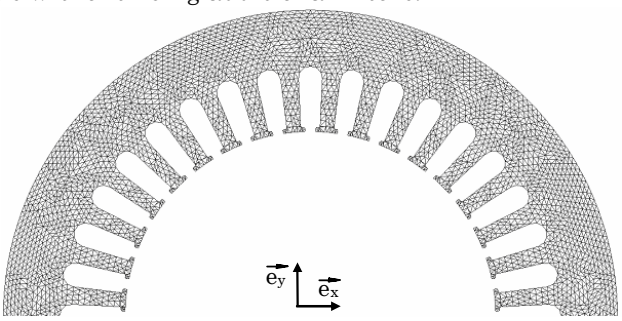

Figure 8. Finite element mesh of the iron stator lamination with 36 slots, a total slot height of 13mm, an average slot width of 4mm, a stator yoke thickness of 11mm and a bore diameter of 75.5mm.

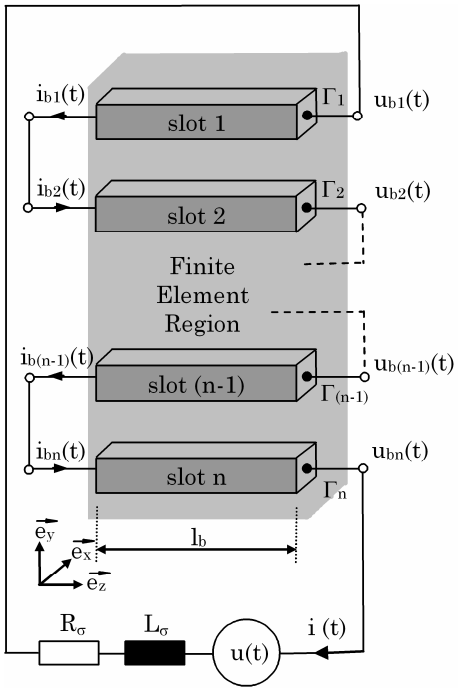

Figure 9. A number of n-serial connected bars, each consisting of 90 single wires inside one slot, are forming one stator coil with 540 windings inside the plane finite element domain, whereas both external parameters $R_\sigma = 7.74\Omega$ and $L_\sigma = 6.4\text{mH}$ are representing 3D stator effects.

III. Field-Circuit Coupling Technique

The local field quantities of the applied 2D finite element algorithm must be coupled to external circuits in order to include the arbitrary source voltage waveforms of the power converter [10].

The finite element representation of the axially un-skewed stator lamination is exemplarily given in Fig.8. The modeling of the voltage-fed stator winding system in Fig.9 generally demands a distinct number of series connected bars in order to form one single coil. The stator phase resistor and the stator phase inductance in Fig.9 represent the not modeled 3D end-winding effects within the 2D finite element calculation [11]. All three stator phases are further star-connected. The supplied voltage at the external terminals in Fig.9 can thereby be arbitrarily varying by time.

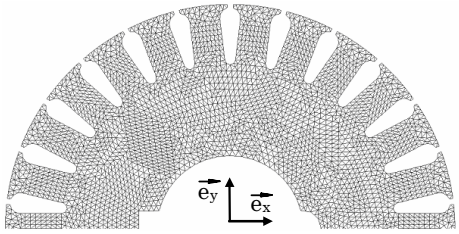

Figure 10. Finite element mesh of the iron rotor lamination with 26 slots, a total slot height of 9.2mm, an average slot width of 2.6mm, a bore diameter of about 75mm, a rotor yoke thickness of 16mm and a shaft diameter of about 25mm.

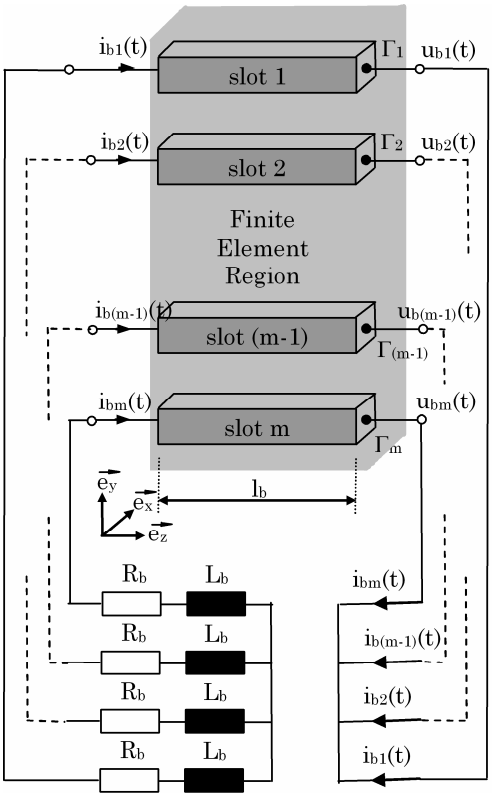

Figure 11. A number of m-parallel connected coils, consisting of aluminum die casting, built up the squirrel cage rotor inside the plane finite element domain, whereas the external parameters $R_b = 1.74\mu\Omega$ and $L_b = 22.5\text{nH}$ are implicit representing 3D end-ring effects.

The exemplarity depicted time-dependent voltage waveform in Fig.6 is governed by very fast rising/falling voltage flanks, which have to be processed within the coupled numerical finite element analysis. Thus, the chosen time-step for solving is often less than 10 ns [12,13].

The used 2D finite element model of the un-skewed rotor depicted in Fig.10 is not suitable to account for 3D end-ring effects. The complete winding schema for the not skewed squirrel cage rotor is shown in Fig.11, whereby the combined parameters approximately take account of 3D influences.

The finite element approach allows the computation of the acting magnetic force on the solid rotor by 'virtual motion' as sum over local contributions [14]. The rotor moves on stepwise with the aid of the applied 'band technique' [15]. Thus, elements which are situated at these band domain may be deformed during motion since some of their nodes may follow the moving rotor reference frame and some the stationary stator one [16]. These element distortions are occurring in dependency on the movement. So, the continuous element distortion enforces a re-meshing of air-gap elements lying on the band.

Due to the non-linear iron material properties, as listed in Table 1, linearization and time-discretization methods are necessary to solve such coupled electromechanical problems in the time domain [17-19].

TABLE I
NON–LINEAR IRON MAGNETIZATION CHARACTERISTIC

B [T]	0	0.4	0.8	1.2	1.6	2.0
H [A/m]	0	140	190	260	1370	20500

IV. TIME-DEPENDENCY OF THE ELECTRIC CURRENT AND THE MECHANICAL TORQUE

The analysis of the time-dependent courses of the electrical current and the mechanical torque within inverter driven motors in the time-domain is of main importance, because it allows further estimations about additionally heating effects as well as critically resonance frequencies of the rotating shaft.

A. Higher harmonics in the electrical current

The numerical analysis of the complete voltage-fed drive system with respect to the course depicted in Fig.6 for a carrier frequency of 2 kHz delivers the time-dependent electrical stator current as depicted in Fig.12. The application of the series-expansion

$$i(t) = \sum_{k=1}^{\infty} \hat{I}_k \sin\left(2\pi k f \cdot t + \alpha_k\right) \qquad (1)$$

delivers all harmonic components $\hat{I}_k$.

Thereby, the distinct fundamental component $\hat{I}_1 = 2.86\,A$ at 50 Hz, and additionally the undesired first side pair harmonics $\hat{I}_{39} = 0.17\,A$ at 1950 Hz and $\hat{I}_{41} = 0.27\,A$ at 2050 Hz as well as the second side pair harmonics $\hat{I}_{79} = 0.05\,A$ at 3950 Hz and $\hat{I}_{81} = 0.08\,A$ at 4050 Hz can be found in the complete spectrum of Fig.13. Higher harmonic contributions are of secondary interest.

The measured electrical current course and the according harmonic analysis are depicted in Fig.14. Not only the comparison of the time-values with those in Fig.12, even though the harmonic magnitudes received from (1) show a good conformity.

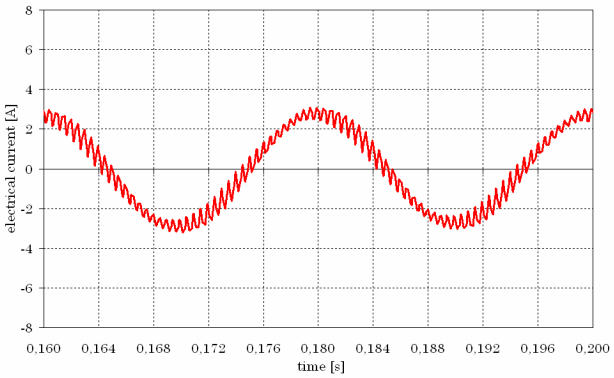

Figure 12. Calculated electrical motor current for a carrier frequency of 2 kHz.

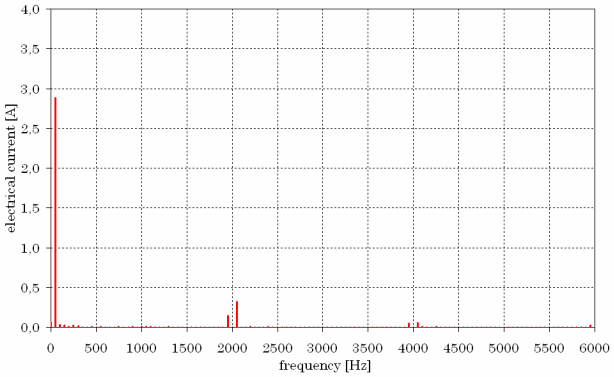

Figure 13. Fourier spectrum of the calculated motor current for a carrier frequency of 2 kHz.

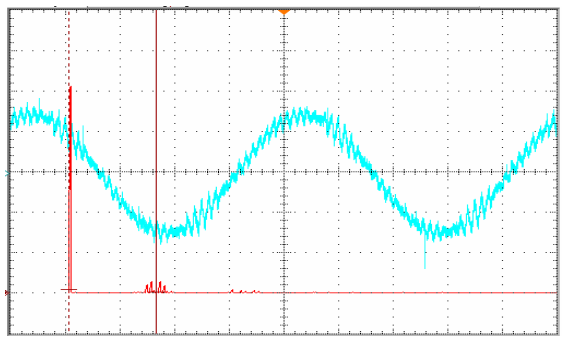

Figure 14. Measured motor current (blue) for a carrier frequency of 2 kHz, whereby one division corresponds to 4 ms in the abscissa and 2 A in the ordinate. The Fourier spectrum (red) is based on 0.6 A per ordinate division.

In spite of some differences between the numerical processed voltage shape in Fig.6 and the measured voltage in Fig.7, in particular during the switching on/off state, no significant discrepancy between the numerical calculated and the measured time-dependent current distribution in Fig.12 and Fig.14, respectively, can be found due to the distinct inductive behavior of the squirrel cage induction motor.

In order to smooth the overlaid current ripple within the distribution in Fig.12, the first harmonic pair in Fig.13 caused by the carrier frequency of 2 kHz has to be eliminated by increasing the frequency to 4.5 kHz.

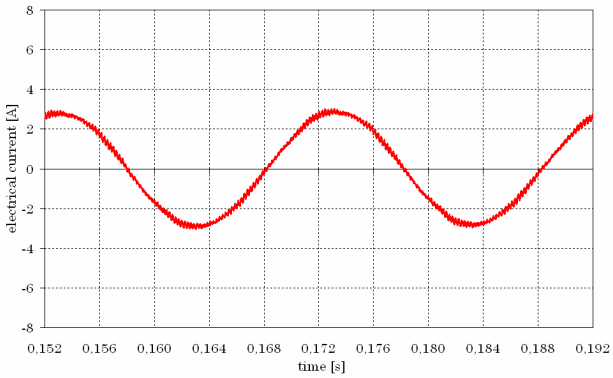

Figure 15. Calculated electrical motor current for a carrier frequency of 4.5 kHz.

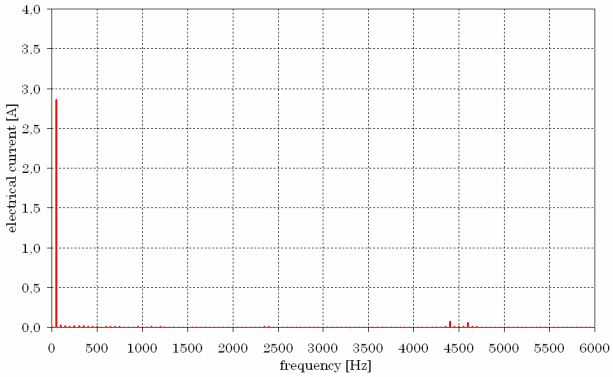

Figure 16. Fourier spectrum of the calculated motor current for a carrier frequency of 4.5 kHz.

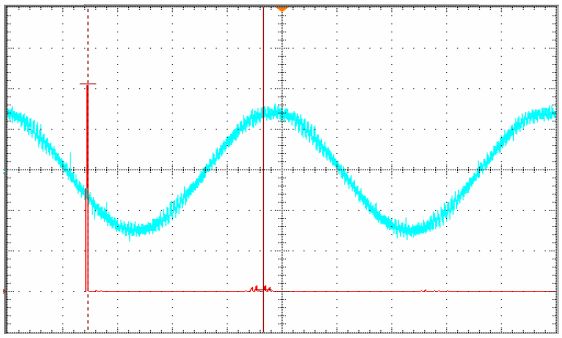

Figure 17. Measured motor current (blue) for a carrier frequency of 4.5 kHz, whereby one division corresponds to 4 ms in the abscissa and 2 A in the ordinate. The Fourier spectrum (red) is based on 0.6 A per ordinate division.

The improvement within the electrical current quality is shown in Fig.15. The course is very similar to the desired sinusoidal one. That circumstances are also obvious from the associated spectrum (1) depicted in Fig.16. Beside the desired fundamental component, only a first sideband with $\hat{I}_{88} = 0.06\,\mathrm{A}$ at 4400 Hz and $\hat{I}_{92} = 0.07\,\mathrm{A}$ at 4600 Hz exists. From a comparison of the numerical calculated results from Fig.15 and Fig.16 with the measured quantities in Fig.17 it is obvious, that a good agreement could be achieved.

B. Higher harmonics in the mechanical torque

The numerical calculated time-dependent mechanical torque is depicted in Fig.18 for a control strategy based on the carrier frequency of 2 kHz. The series-expansion

$$m(t) = \sum_{k=0}^{\infty} \hat{M}_k \sin\left(2\pi k f \cdot t + \beta_k\right) \qquad (2)$$

leads to the harmonic magnitudes $\hat{M}_k$, which are further shown in Fig.19. Beside the desired constant contribution of $\hat{M}_0 = 4.9\,\mathrm{Nm}$, a very distinct undesired torque fluctuation due to the converter topology of Fig.3 is caused by the component $\hat{M}_{42} = 0.45\,\mathrm{Nm}$ at 2100 Hz Other contributions to the torque ripple are obviously suppressed.

An improved spectrum could be achieved by increasing the carrier frequency up to 4.5 kHz. The analysis of the numerical results from Fig.20 in the frequency domain results to the torque spectrum shown in Fig.21. The previously torque components are shifted to higher ordinal numbers at 4500 Hz with lower magnitude $\hat{M}_{90} = 0.2\,\mathrm{Nm}$. A comparison of Fig.18 with Fig.20 shows that effect imposingly.

Thus, undesired effects concerning the quality of the true shaft motion of the drive system could be avoided by using higher carrier frequencies.

V. Conclusion

The prediction of undesired current and torque harmonics inside converter-fed induction motors is of crucial interest in order to guarantee a high quality level of the drive system. Thereby, the complex interaction of the converter and the squirrel cage induction motor has to be considered. This is done by using the 2D transient electromagnetic-mechanical finite element method with additionally coupled external circuits. Fortunately, the generated arbitrary time-dependent output voltage waveforms of the converter are directly processed within the non-linear finite element analysis in the time-domain. Effects of minor changes in the mechanical rotor true running due to the torque ripple as well as fluctuations in the electrical current consumption are regarded.

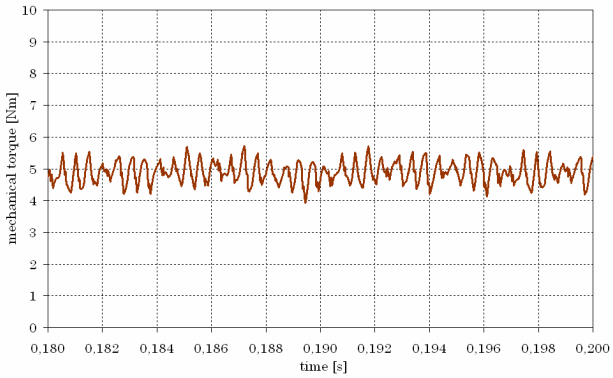

Figure 18. Calculated mechanical torque for a carrier frequency of 2 kHz.

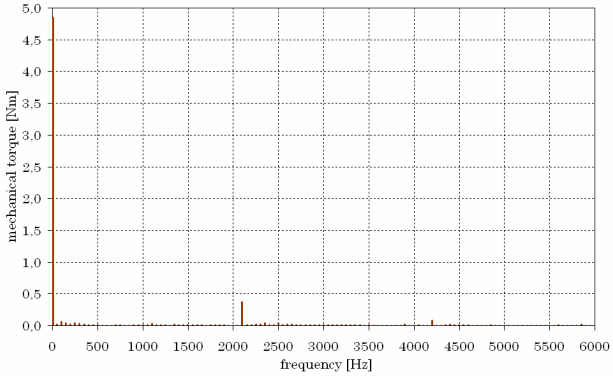

Figure 19. Fourier spectrum of the calculated mechanical torque for a carrier frequency of 2 kHz.

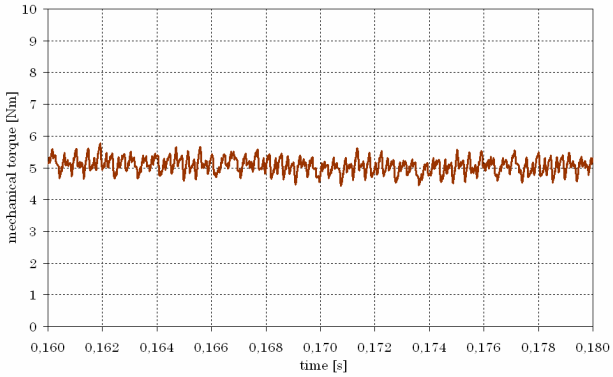

Figure 20. Calculated mechanical torque for a carrier frequency of 4.5 kHz.

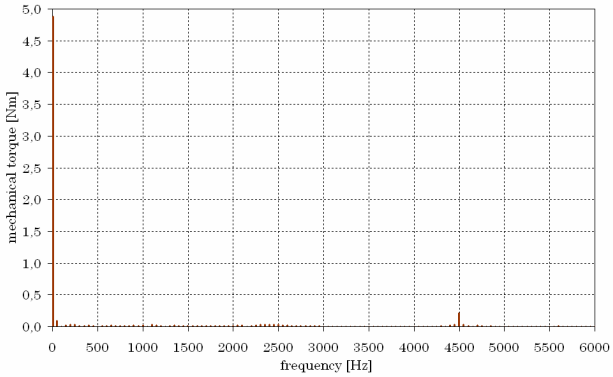

Figure 21. Fourier spectrum of the calculated mechanical torque for a carrier frequency of 4.5 kHz.

REFERENCES

[1] K. Heintze, H. Tappeiner and M. Weibelzahl, *Pulswechselrichter zur Drehzahlsteuerung von Asynchronmaschinen*, Siemens Zeitschrift 45, Heft 3, 1971.

[2] T.A. Lipo, P.C. Krause and H.E. Jordan, *Harmonic Torque and Speed Pulsation in a Rectifier-Inverter Induction Motor Drive*, IEEE Transactions on Power Apparatus and Systems, Vol. PAS-88, No.5, 1969.

[3] D.T. Stuart and K.M. Hebbar, *Torque Pulsation in Induction Motors with Inverter Drives*, IEEE Transactions on Industry and General Applications, Vol. IGA-7, No. 2, 1971.

[4] A. Heimbrock and H.O. Seinsch, *Neue Erkenntnisse über Oberschwingungsverluste in Umrichtergespeisten Käfigläufern*, Elektrotechnik und Informationstechnik, 122. Jahrgang, Heft 7/8, 2005.

[5] I. Szabo, *Technische Mechanik*. Berlin Heidelberg New York: Springer Verlag, 1972.

[6] H. Kleinrath, *Stromrichtergespeiste Drehfeldmaschinen*, Springer Verlag: Wien, 1980.

[7] G.S. Buja and G.B. Indri, *Optimal Pulse Width Modulation for Feeding AC Motors*, IEEE Transactions on Industry Applications, Vol. IA-13, No.1, 1977.

[8] G.B. Kliman and A.B. Plunkett, *Development of a Modulation Strategy for a PWM Inverter Drive*, IEEE Transactions on Industry Applications, Vol. IA-15, No. 1, 1979.

[9] J.M.D. Murphy and M.G. Egan, *A Comparison of PWM Strategies for Inverter-Fed Induction Motors*, IEEE Transactions on Industry Applications, Vol. IA-19, No. 3, 1983.

[10] P.P. Silvester, *Finite Elements for Electrical Engineers,* Kluwer Academic Publisher: Boston/London, 1995.

[11] J.S. Salon, *Finite Element Analysis of Electrical Machines,* Cambridge University Press: Cambridge, 1996.

[12] B. Istfan, *Extensions to the Finite Element Method for Nonlinear Magnetic Field Problems*, PhD Thesis Rensselaer Polytechnic Institute, New York, 1987.

[13] O. Biro, K. Preis and K.R. Richter, *"On the Use of the Magnetic Vector Potential in the Nodal and Edge Finite Element Analysis of 3D Magnetostatic Problems," IEEE Transactions on Magnetics,* vol. 32, no. 5, 1996.

[14] M.J. DeBortoli, *Extensions to the Finite Element Method for the Electromechanical Analysis of Electrical Machines, PhD Thesis,* Rensselaer Polytechnic Institute, New York, 1992.

[15] B. Davat, Z. Ren and M. Lajoic-Mazenc, *The movement in field modeling*, IEEE Transactions on Magnetics, Vol. 21, No. 6, 1985.

[16] R. Palma, *Transient Analysis of Induction Machines using Finite Elements, PhD Thesis,* Rensselaer Polytechnic Institute, New York, 1989

[17] K.J. Bins, P.J. Lawrenson and C.W. Trowbridge, *The Analytical and Numerical Solution of Electric and Magnetic Fields,* John Wiley & Sons: Chichester, 1992.

[18] K.J. Bathe, *Finite Element Procedures*, Prentice Hall: New Jersey, 1996.

[19] R. Schwarz, *Methode der Finiten Elemente*, B. G. Teubner: Stuttgart, 1984.